ACS Electrochemistry

Open Access

This article is licensed under CC-BY 4.0

pubs.acs.org/electrochem

Article

Early Chronoamperometric Transients Extraction Improves Sensitivity for Electrochemical Immunosensors

Niamh Docherty, Ashton Theakstone,† Dominik Duleba, Matthew J Baker,† Robert P. Johnson, and Damion K. Corrigan*

Cite This: https://doi.org/10.1021/acselectrochem.6c00175

Read Online

ACCESS | Metrics & More | Article Recommendations | Supporting Information

ABSTRACT: Chronoamperometric biosensors are simple and robust but often the lack sensitivity required to detect low abundance analytes. Conventional chronoamperometry analysis relies on the limiting current, which is often compromised by background currents and poor discrimination between target-specific and nonspecific signals. Here, the extraction and integration of the information-rich early transient improve sensitivity gains and reduce measurement speed. A chronoamperometric electrochemical immunoassay for cardiac troponin I (cTnI) was used as a model system. Current−time traces were analyzed via integration to obtain the area under the curve (AUC), with integration windows defined using either fixed time intervals or a novel gradient-based thresholds. The gradient-based method dynamically selects regions of the transient based on the rate of current change, isolating the kinetically informative signal without requiring prior knowledge of optimal time windows. This approach reduced the limit of detection (LOD) from 130 to 80 pg mL^{-1} for chemisorbed sensors and from 233 to 40.4 pg mL^{-1} for physisorbed systems, while comparable sensitivity was observed for a plate-based format (1000−1018 pg mL^{-1}). These results show that early transient analysis is most effective when redox activity is localized near the electrode surface and leads to similar results for diffusion-limited systems. This data-driven framework enhances sensitivity without modifying assay chemistry or hardware, offering a practical route toward faster, low-cost, and sensitive amperometric biosensing.

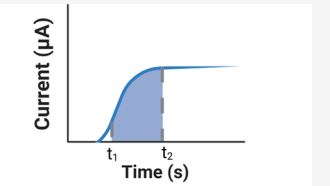

Transient analysis improves sensitivity

KEYWORDS: *chronoamperometry, amperometric immunosensors, chronoamperometric analysis*

INTRODUCTION

Enzyme-labelled immunosensors often utilize chronoamperometry, with personal glucose meters serving as a prominent example.[1−3] Enzyme labels are used to produce a redox active species from an enzyme substrate.[4] Despite widespread adoption, enzymatic amperometric biosensors struggle to achieve the ultra-sensitive detection limits. Alternatives such as voltammetric and impedance-based methods often provide enhanced sensitivity by resolving interfacial kinetics and charge-transfer resistance with greater precision.[5,6] However, these methods involve instrumentation complexity and longer analysis times, hindering translation into point-of-care or high-throughput diagnostic formats.[7]

Chronoamperometry measures the time-dependent current when a constant potential is applied, thereby inducing reduction or oxidation of an electroactive species in solution. The current-time trace is characterized by an initially high current due to the availability of electroactive species at the electrode surface, followed by current decay as this local concentration is depleted. Over time, the system transitions to a diffusion-controlled regime, where a concentration gradient forms between the bulk solution and the electrode surface, leading to a limiting current. The analytical information contained within a chronoamperometric transient can vary with time. Typically, current-time responses consist of time-dependent contributions from both faradic and non-faradic charging at the electrode−electrolyte interface. Under ideal diffusion conditions, the faradic component follows the $t^{-1/2}$ dependence described by the Cottrell equation, while the capacitive charging contribution is a more rapidly decaying response.[8]

Conventionally, the limiting current is used as the detection signal, with higher analyte concentrations producing larger currents due to increased concentration of redox-active species diffusing to the electrode surface.[9−12] While widely adopted, the limiting current is influenced by slow mass transport and background processes and requires extended acquisition times.[8,13] Additionally, the current response is influenced by the electrode material, size, bioreceptors and immobilization chemistry. The immobilization chemistry governs electron transfer efficiency, enzymatic turnover, mass transport, and the density, orientation, and activity of immobilized components, all of which directly affect both transient and limiting current signals.[14]

Received: April 24, 2026
Revised: August 24, 2026
Accepted: October 12, 2026

Downloaded from pubs.acs.org/aecic7/article-pdf/doi/10.1021/acselectrochem.6c00175/6909763/ec-2026-00175f.pdf by guest on 06 November 2026

© XXXX The Author(s). Published by American Chemical Society

This is particularly troublesome for assays designed to detect low-abundance proteins in complex samples. As a result, calibration, validation, and sensitivity challenges continue to limit the broader application of chronoamperometry in high-performance biosensing.[4] Sensitivity gains are therefore typically pursued through changes to the sensor itself. For example, 3D-printed microelectrodes with off-electrode antibody immobilisation achieved lower LODs using the limiting current, largely through improved antibodies and electrode design.[15]

Early-time transient currents contain enriched information as established by classical electrochemical theory.[16] Transient-based analysis improves robustness, shortens measurement times, and, in some cases, eliminates the need for calibration.[17] Specifically, area under the curve (AUC) analysis has been shown to provide a sensitive, time-efficient metric in electrochemical impedance spectroscopy.[18] However, these strategies have yet to be applied to enzymatic chronoamperometric assays or compared to limiting current analysis. Consequently, it is unclear whether optimizing transient regions can enhance sensitivity, signal reliability, and measurement speed in practical amperometric biosensing formats.

Chronocoulometry provides a closely related framework in which the current following a potential step is integrated with respect to time to obtain charge. It has been widely used for the characterization and quantification of surface-confined species, including immobilized DNA, and has also been applied to electrochemical immunoassays.[19−21] In the present work, rather than simply integrating charge over a predefined measurement interval, we investigate whether analytically informative regions of the chronoamperometric transient can be identified and selectively integrated. We demonstrate that gradient-defined integration of the early transient can enhance analytical sensitivity and that the magnitude of this improvement depends upon the assay architecture and localization of the electroactive product.

Using cardiac troponin I (cTnI) as a model analyte, we systematically evaluate the use of AUC analysis over short timescales as an alternative quantification strategy. Full-time AUC integration was performed to compare the chronoamperometry to chronocoulometric analysis to establish whether integrating the entire transient offers an analytical advantage. We then refine this approach by applying fixed early-time integration windows (e.g., 0.1−1 s), targeting the initial current decay where signal-to-background contrast is greatest. A framework was established to enable customization and optimization of the selected time window by utilizing a gradient-based threshold selection of data for AUC calculations (Figure 1). To assess the robustness and mechanistic relevance of gradient threshold screening and AUC data analysis strategy, the approach was further evaluated across multiple antibody immobilization strategies, allowing the study of how surface chemistry and mediator distribution influence transient signal formation and the resulting analytical performance.

This work indicates that integrating the early, kinetically informative region of the chronoamperometric response systematically unlocks substantial improvements in sensitivity while reducing measurement time. Importantly, this enhancement is achieved solely through data analysis, without altering assay chemistry or hardware. These findings highlight the potential of gradient-informed AUC analysis as a simple yet powerful strategy to improve the performance and translational potential of amperometric biosensors in clinical diagnostics, environmental monitoring, and point-of-care applications.

MATERIALS AND METHODS

Electrochemical ELISA Data Collection

The datasets were produced from a cTnI amperometric immunosensor using thin-gold film electrodes. Further details can be found in Supporting information and or previous work.[11]

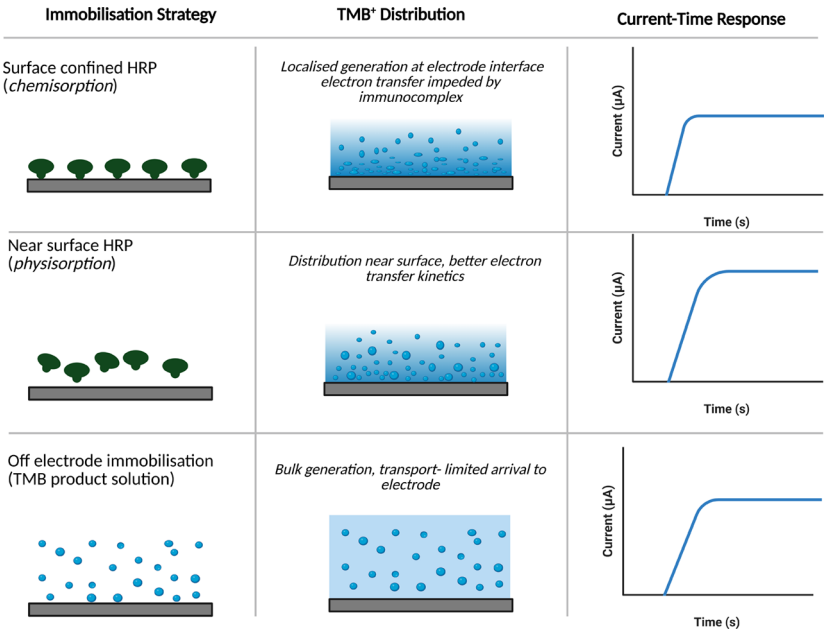

Figure 1. Schematic representation of how immobilization strategy and resulting redox active product (TMB^+) distribution influence electron transfer kinetics and temporal response. When HRP is confined at the electrode surface (chemisorption), TMB^+ is generated locally, producing rapid electron transfer characterized by a steep early-time decay gradient. Increasing the separation between enzyme and electrode (physisorption) broadens the TMB^+ distribution and introduces diffusion limitations, yielding a slower initial decay. Off-electrode generation results in transport-limited delivery of TMB^+, producing a further reduction in decay rate and a distinct quasi-steady-state current.

Downloaded from pubs.acs.org/aecic7/article-pdf/doi/10.1021/acselectrochem.6c00175/69097663/ec-2026-00175f.pdf by guest on 06 November 2026

https://doi.org/10.1021/acselectrochem.6c00175
ACS Electrochem. XXXX, XXX, XXX−XXX

Electrochemical measurements were performed using a PalmSens4 potentiostat equipped with an MUX8-R2 multiplexer and controlled via PSTrace 5.9. Thin gold-film electrode arrays (TGF-E8; FlexMedical Solutions, UK) were used as the sensing platform; each array comprised eight laser-ablated gold working electrodes on a sputtered polyester substrate with an integrated Ag/AgCl reference electrode. Immediately prior to use, electrodes were cleaned by cyclic voltammetry in 100 mM H_2SO_4, cycling between 0 and 1.6 V (vs Ag/AgCl) at 300 mV/s until stable overlapping scans were obtained (16 cycles). Human serum was filtered through a 0.2 μm filter syringe, and 1 in 10 dilution was performed using reagent diluent. Diluted human serum was prepared as the diluent in cTnI standards (125−8000 pg mL^{-1}).

Electrochemical ELISA: Well-to-Electrode Format

A conventional plate-based ELISA was performed to benchmark assay performance. Capture antibody (2 μg mL^{-1}) was immobilized on 96-well plates overnight, followed by blocking, incubation with cTnI standards, detection antibody, streptavidin−HRP, and TMB substrate. Following completion of the 20 min TMB substrate incubation, the supernatant was transferred directly from the plate to cleaned TGF-E8 electrodes. Chronoamperometry was performed at −0.2 V for 60 s (0.1 s interval) across all eight working electrodes.

Electrochemical ELISA: Physisorption Format

Capture antibody (12 μg mL^{-1}) was physically adsorbed onto cleaned electrodes overnight at 4 °C. After blocking, electrodes were incubated with cTnI standards for 90 min, followed by detection antibody and streptavidin−HRP. TMB substrate was applied for 20 min before chronoamperometry at −0.2 V for 60 s.

Electrochemical ELISA: Chemisorption Format

Capture antibody (200 μg mL^{-1}) was thiolated using 40 mM sulfosuccinimidyl 6-(3′-(2-pyridyldithio) propionamido) hexanoate (sulfo-LC-SPDP) and reduced with 150 mM DTT in 5× PBS before immobilization onto the gold surface overnight at 4 °C. After blocking with 1 mM MCH, electrodes were incubated with cTnI or control standards (in reagent diluent or 10% serum), followed by detection antibody (800 ng mL^{-1}) and streptavidin−HRP. After TMB incubation (20 min), chronoamperometry was performed at −0.2 V for 45 s.

To avoid noise amplification during numerical differentiation, the gradient was not computed from instantaneous point-to-point differences. Instead, current changes were evaluated over fixed 0.1 s intervals, which acts as a low-pass temporal averaging step and suppresses high-frequency noise.

Area Under the Curve Using Time Interval Cutoffs

Data were exported from PSTrace to MATLAB, where the AUC was determined using the trapezoidal rule and plotted against cTnI concentration. Each AUC value was computed per replicate ($n = 8$) across all concentrations (125−8000 pg mL^{-1} cTnI standards) and the negative control (8000 pg mL^{-1} MMP3 standard). The AUC analysis was repeated with various fixed windows (0.1−1, 0.1−2, 0.1−5, 0.1−10, 0.1−15, 0.1−30, and 0.1−45 s) to compare with full window integration and the previous sensitivity obtained using the steady state/limiting current. Calibration and LOD determination were performed as described in Section 2.4.

Gradient Analysis of Current−Time Traces

To capture the dynamic features of the chronoamperometric response, the gradient of each current−time profile was first evaluated. Chronoamperometric data were processed in MATLAB, and the first derivative of current with respect to time (dI/dt) was calculated at 0.1 s intervals. The resulting gradient−time profiles were examined to characterize signal evolution and to inform the selection of gradient ranges for subsequent analysis.

Gradient-Based Optimization via Heatmap Analysis and Combined Performance Score

Gradient-based thresholds were systematically optimized to assess the robustness of the analysis and identify the ideal gradient cutoff pair. A matrix of lower and upper gradient cutoffs was defined based on the gradient-time profile observed for each dataset. For each cutoff pair, the corresponding segments of the transient were isolated and integrated to calculate the AUC.

Each gradient threshold combination generated an independent calibration dataset (AUC versus concentration), which were analysed individually. See Section 2.6 for further details on model fitting and LOD calculations.

Analytical performance metrics, including LOD, coefficient of variation (CoV), signal-to-noise ratio (SNR), and coefficient of determination (R^2), were calculated for each cut-off pair. To visualize the effect of gradient thresholds, heatmaps were generated in MATLAB, where colour intensity represented the numerical value of each performance metric, enabling direct comparison across the parameter space.

A composite performance score was then calculated by normalizing and equally weighting the four metrics (LOD = 0.25, CoV = 0.25, SNR = 0.25, $R^2 = 0.25$). The gradient cutoff pair with the highest composite score was selected as the optimal region, representing the best balance between sensitivity, repeatability, signal robustness, and model fit quality.

AUC Methodology Validation—Comparison of Bulk Solution vs Physisorption vs Chemisorption

In previous work, three cTnI Immunosensors were compared using three different electrode immobilization strategies (Table 1). (i) For chemisorption, sulfo-LC-SPDP was used as a crosslinker to enable covalent attachment of the primary antibody to the electrode surface, after which the on-electrode electrochemical immunoassay was carried out following the same steps as the physisorption approach. (ii) For physisorption, capture antibodies (12 μg mL^{-1}) were incubated directly on the thin gold film electrode surface overnight at 4 °C in a humidity chamber, with the remainder of the electrochemical immunoassay protocol performed on-electrode, including gentle washing with 1× PBS between steps. (iii) For the plate-based format, the ELISA was first completed conventionally in a 96-well plate, and following TMB substrate incubation, the solution was transferred to clean electrodes for electrochemical measurement.

The total AUC was calculated for each replicate across all experiments and visualized using boxplots to compare signal variation between immobilization strategies. To ensure fair comparison of the TMB-specific signal, each dataset was normalized to its corresponding blank response. Calibration curves were produced from the normalized AUC values to compare the signal magnitude and variability between immobilization strategies. Signal variability was quantified as the relative standard deviation (RSD) across replicates, allowing reproducibility to be compared independently of signal magnitude. The relationship between signal magnitude and reproducibility was further assessed by plotting mean RSD against mean total AUC for each concentration.The gradient based threshold screening and calibration curves of the optimal cutoffs were produced for comparison with the chemisorption dataset and the limiting current data analysis approach.

Table 1. Experimental Conditions and Limit of Detection of cTnI Electrochemical ELISA Data sets

antibody immobilization	sample diluent	LOD (pg mL^{-1})
chemisorption	10% human serum	130
physisorption	10% human serum	233
well to electrode	1 % BSA	1000

Downloaded from pubs.acs.org/aecic7/article-pdf/doi/10.1021/acselectrochem.6c00175/6909763/ec-2026-00175f.pdf by guest on 06 November 2026

https://doi.org/10.1021/acselectrochem.6c00175
ACS Electrochem. XXXX, XXX, XXX−XXX

Data Fitting and LOD Calculations

Calibration data were analysed using both a four-parameter logistic (4PL) model and log−log linearization. 4PL fitting is used in figures comparing against conventional limiting current analysis to enable direct comparison with standard immunoassay calibration. While 4PL fitting is the conventional approach for immunoassay calibration, the full sigmoidal response was not consistently captured across the investigated concentration range, resulting in poorly constrained fits. Both models were therefore applied to all datasets, with interpretation based on the model that best represents the observed data shape.

For gradient threshold screening, using log−log linearization was used as the default to ensure consistent comparison across cut-off thresholds. Where sigmoidal behaviour was observed (e.g., in plate-based assays), 4PL model was applied where appropriate. Both curve-fitting approaches are reported throughout.

The LOD was defined in accordance with the IUPAC definition, where the signal threshold was defined as the mean blank response plus three times its standard deviation (LOD_signal = $\bar{S}$_blank + 3σ_blank). The corresponding concentration was obtained by inverting the selected calibration model.

Uncertainty in the LOD was estimated by propagation of uncertainty following the ISO Guide to the Expression of Uncertainty in Measurement (GUM). Uncertainty in the signal threshold was derived from the uncertainty in the blank mean and standard deviation and propagated through the inverse calibration model. For log−log linear models, uncertainty in the fitted slope and intercept, including covariance, was included. For 4PL models, uncertainty was propagated through the inverse 4PL function where parameter covariance information was available. Where 4PL fitting was applied, LOD uncertainty was estimated by propagation through the inverse 4PL function when fit parameter uncertainty information was available. However, because some datasets did not fully constrain the sigmoidal response, log−log linearization was used as the primary basis for screening and for datasets lacking a well-defined upper plateau. Final LOD values are reported as LOD±u_{LOD}.

To evaluate sensitivity improvements, the percentage change in LOD relative to the steady-state method was calculated:

$$\%\Delta\mathrm{LOD} = \frac{\mathrm{LOD_{method}} - \mathrm{LOD_{steady-state}}}{\mathrm{LOD_{steady-state}}} \times 100$$

This comparison allowed direct evaluation of how gradient-dependent analyses influenced assay linearity, uncertainty, and overall detection performance across adsorption regimes.

Overview of Gradient Threshold Selection for AUC Analysis

Figure 2 summarizes the workflow principle for gradient-based thresholds to determine the AUC most representative of the current time response. This approach enables adaptive extraction of early-time kinetic information that is not captured by fixed-time or steady-state analysis.

RESULTS AND DISCUSSION

Limitations of Steady-State Current and Fixed Time-Window AUC Analysis

Figure 3A depicts prior work which obtained an LOD of 130 pg mL^{-1} after extracting the limiting current at the final time point (45 s). This detection limit was used as a benchmark for comparison with alternative analysis strategies.

Next, AUCs were calculated over multiple fixed intervals and plotted against concentration to generate calibration curves and corresponding LODs. Figure 3B shows the full integration window (0.1−45 s), while Figure 3C presents shorter intervals (0.1−1, 0.1−5, 0.1−10, and 0.1−15 s). Resulting LODs for each time interval and fitting approach are summarized in Table 2 and calibration curves are available in the Supporting Information.

LODs obtained using 4PL fitting ranged from 106.93 ± 21 to 127.50 ± 27 pg mL^{-1}, while log−log linearization yielded LODs between 107.43 ± 21 and 138.19 ± 29 pg mL^{-1}. As a complete sigmoidal response was not observed across the investigated concentration range, the 4PL model is less well suited. Therefore, the log−log linear fit is considered to provide a more reliable and robust estimate of LOD under these conditions.

A modest improvement in LOD was observed at longer integration times, with the lowest LOD values obtained at 0.1−45 s for the 4PL model (106.93 ± 21 pg mL^{-1}) and at 0.1−30 s for the log−log model (107.43 ± 21 pg mL^{-1}). The LODs were

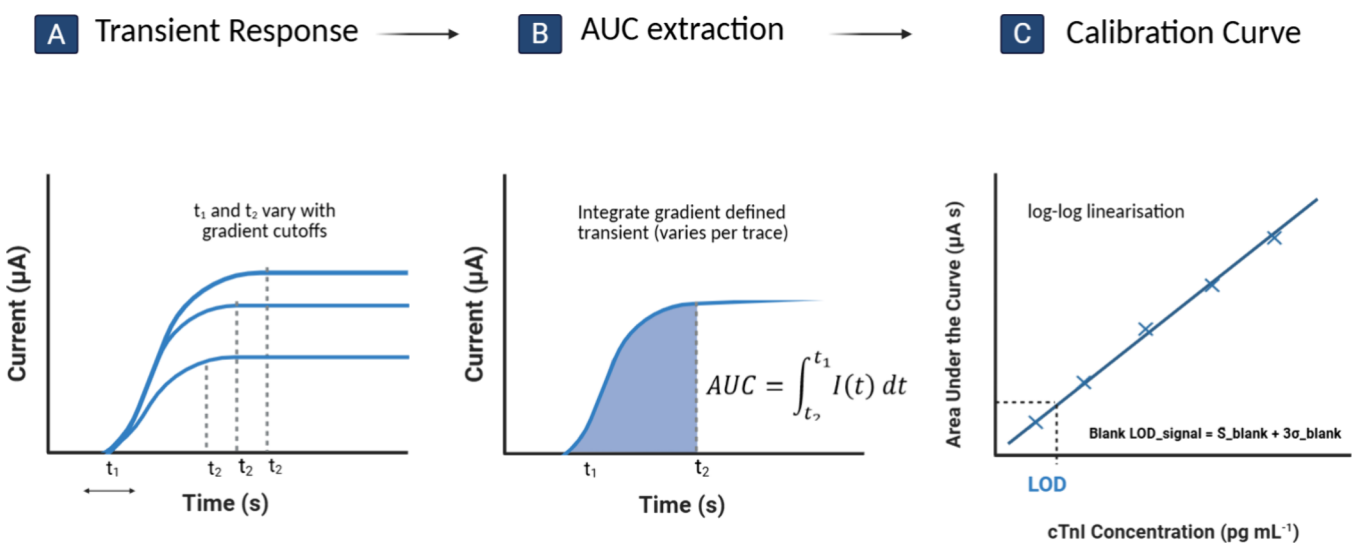

Figure 2. Data analysis pipeline for gradient-based AUC extraction. (A) Representative current−time transients are obtained from chronoamperometric measurements. Gradient thresholds are applied to identify the kinetically informative region of each transient. (B) Area under the curve (AUC) is calculated for each trace within the selected region, where the integration bounds (t_1 and t_2) vary dynamically depending on the local gradient of each current−time response. (C) Mean AUC values at each concentration are used to construct calibration curves.

Downloaded from pubs.acs.org/aecic7/article-pdf/doi/10.1021/acselectrochem.6c00175/6909763/ec-2026-00175f.pdf by guest on 06 November 2026

https://doi.org/10.1021/acselectrochem.6c00175
ACS Electrochem. XXXX, XXX, XXX−XXX

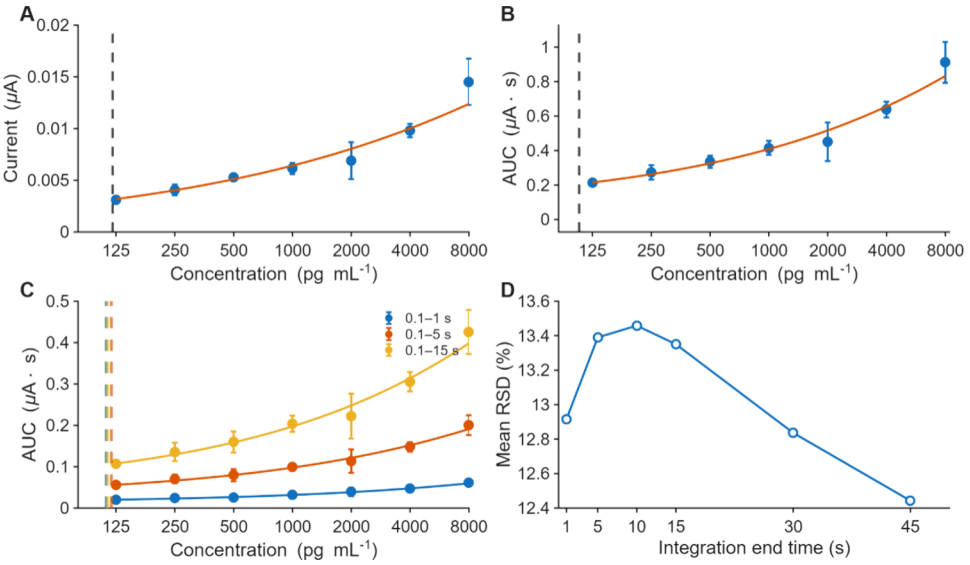

Figure 3. Comparison of limiting current and AUC data analysis. (A) Dose−response curve for limiting current against cTnI concentration. (B) Dose−response curve of AUC between full measurement duration (0.1−45 s). (C) Dose−response curve with shorter fixed time windows. Dose−response curves for both fitting approaches are provided in the Supporting Information (Figures S1.1−S1.6). (D) Mean relative standard deviation of each AUC interval time examined, stating the end time of each fixed window. Calibration curves fitted using a 4PL model to enable direct comparison with conventional immunoassay analysis. In panels (A−C), the dashed line represents the calculated LOD concentration, calculated as the mean of the control samples + 3*std. Error bars are 1 × std.

Table 2. Time-Resolved Integration of Amperometric Biosensor Data[a]

start time	end time	4PL fit LOD (pg mL^{-1})	linear fit LOD (pg mL^{-1})
0.1	1	112.24 ± 28	138.19 ± 30
0.1	5	118.46 ± 24	131.86 ± 27
0.1	10	127.50 ± 27	115.32 ± 22
0.1	15	112.20 ± 21	124.02 ± 27
0.1	30	119.05 ± 27	107.43 ± 21
0.1	45	106.93 ± 21	117.61 ± 28

[a]All time intervals begin at $t_1 = 0.1$ and t_2 varies from 1 to 45 s.

slightly lower than the limiting current benchmark (~130 pg mL^{-1}). Figure 3D shows RSD values remained consistent across integration windows, with only minor variation at intermediate time ranges, indicating that extending the integration window improves sensitivity and variability compared to the fixed short time intervals.

This behaviour reflects the cumulative nature of AUC analysis, where longer integration periods increase total charge collection and average out short-term stochastic fluctuations. This principle is conceptually analogous to pharmacokinetic AUC analysis, where total drug exposure reflects cumulative biological effect rather than a single time-point measurement.[22] However, extended integration times incorporate baseline drift or signal saturation, reducing sensitivity to concentration-dependent differences in the early transient. Fixed integration windows do not account for variations in signal onset, rate of change, or time to plateau, which differ between samples due to factors such as analyte concentration and electrode variability. Therefore, subsequent analysis focused on automatically isolating the initial transient region in each measurement.

Gradient-Based AUC Analysis Enhances Analytical Performance through Kinetic Signal Isolation

Figure 4A shows that the time required to reach a limiting current varies with analyte concentration, with higher concentrations exhibiting a more prolonged decay. This behaviour is reflected in the corresponding gradient−time profiles (Figure 4B), where both the magnitude and duration of the gradient increase with concentration. Peak gradients increased from ~0.08−0.1 nA s^{-1} at low concentrations to ~0.2 nA s^{-1} at 8000 pg mL^{-1}, representing a two-fold increase across the range. In addition, higher concentrations maintained non-zero gradients over longer time periods (>1 s), whereas lower concentrations approached near-zero gradients within ~0.5−0.7 s. Based on these observations, integration could be restricted to regions where the gradient falls within defined bounds, thereby excluding both the initial capacitive spike (high $|dI/dt|$) and the later steady-state region (low $|dI/dt|$). This isolates the kinetically informative portion of the signal associated with concentration-dependent TMB^+ reduction, removing reliance on predefined time points.

Immediately following a potential step, the measured chronoamperometric current contains contributions from both electrical double-layer charging and the reduction of TMB^+. These contributions exhibit different time dependencies, with the capacitive contribution expected to be greatest during the initial rapidly changing region of the transient. The gradient-based approach evaluates these contributions, yet integration can be restricted to regions where the gradient falls within defined bounds, automatically excluding the initial negative magnitude likely resulting from potentiostat sampling, and the greatest contribution from capacitive charging, as well as the later low-gradient region approaching steady state. The resulting window captures the concentration-dependent evolution of the transient while accounting for both faradaic and non-faradaic contributions to the measured signal, without reliance on predefined time points.

Downloaded from pubs.acs.org/aecic7/article-pdf/doi/10.1021/acselectrochem.6c00175/6909763/ec-2026-00175f.pdf by guest on 06 November 2026

https://doi.org/10.1021/acselectrochem.6c00175
ACS Electrochem. XXXX, XXX, XXX−XXX

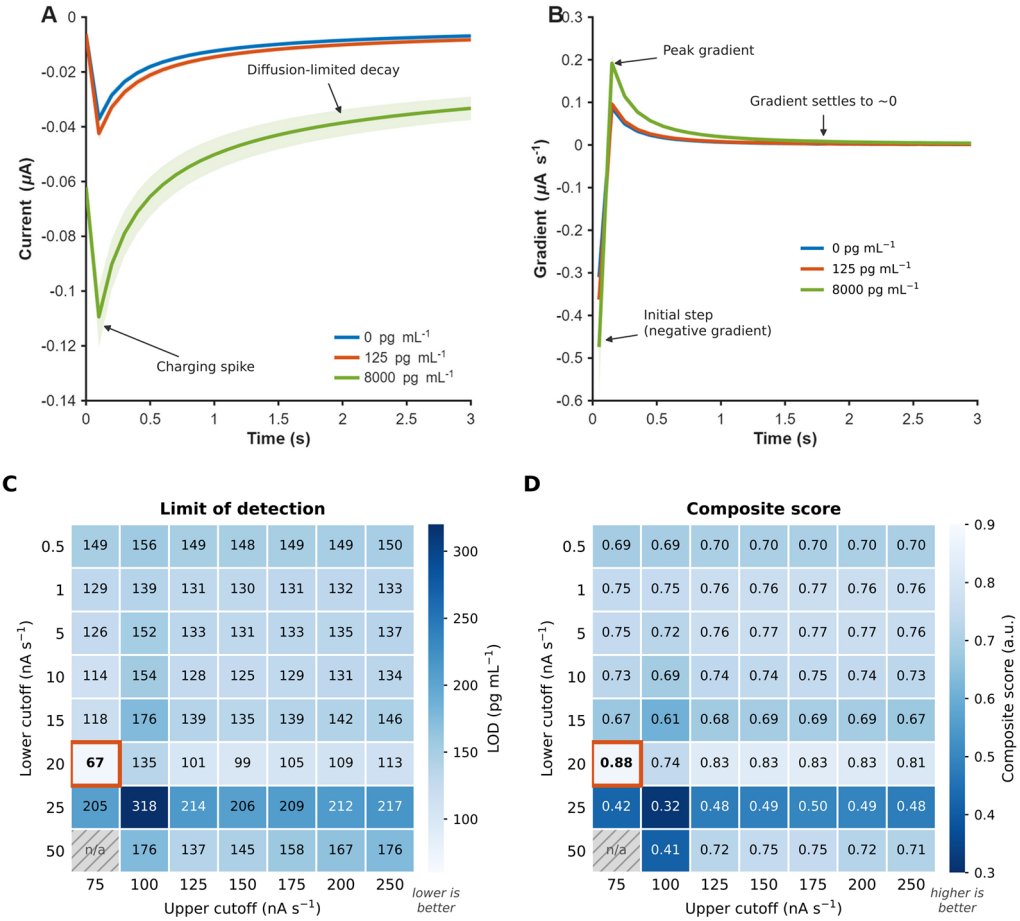

Figure 4. Gradient-based signal optimization for electrochemical troponin detection. (A) Mean chronoamperometric current over the first 3 s for 0, 125, and 8000 pg mL^{-1} cTnI, showing the initial charging spike followed by diffusion-limited decay. (B) Mean current gradient over the same period. (C) LOD heatmap as a function of lower and upper gradient cutoffs, illustrating an optimal operating region. (D) Composite performance heatmap to determine the optimal operating range for gradient-based cutoff. The composite score combines LOD, CV, SNR and *R*-squared values. The outlined cell (lower 20 nA s^{-1}, upper 75 nA s^{-1}) is the optimal operating point, with the lowest LOD (67 pg mL^{-1}) and the highest composite score (0.88). n/a: gradient window too narrow to contain sufficient data points for calibration. Shaded regions in A and B show ±1 SD (n = 8); where not visible, they are narrower than the line width.

A broad range of cutoff candidates were evaluated and indicated similar performance. The LOD heatmap in Figure 4C demonstrated that the lowest LOD values occurred when the lower gradient cut-off was maintained near 20 nA s^{-1}, indicating improved sensitivity at minimal baseline drift thresholds. The composite performance heatmap (Figure 4D) identified the optimal operating region between 20−75 nA s^{-1}. Additional heatmap analyses for CoV, SNR, and R^2 are provided in the Figure S7. Based on these outcomes, a final gradient window of 20−75 nA s^{-1} was selected and applied for subsequent evaluation of chemisorption biosensor responses using the serum dataset (Figure 5).

The gradient cutoff with the highest sensitivity was 20−75 nA s^{-1}, yielding an LOD of 80.0 ± 18 pg mL^{-1}, a significant improvement from the limiting current approach (130 pg mL^{-1}) and the short fixed-time-window integration approach (LOD ∼138 pg mL^{-1}). These results confirm using gradient cut-off for each replicate to the optimal gradient thresholds improves sensitivity more than using fixed short-time integration windows.

Validation of Gradient-Based AUC Integration

To evaluate the generalizability of the gradient-based AUC method, the analysis was applied to two additional configurations: physical adsorption of antibodies onto gold electrodes

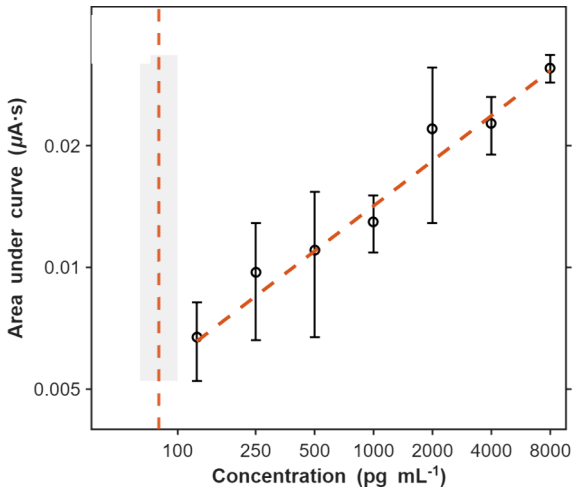

Figure 5. Final dose−response curve obtained using the optimized cutoff parameters (20−75 nA s^{-1}) for the chemisorption-based electrochemical ELISA dataset. Data are presented as mean ± 1 × SD (error bars) (n = 8). Log−log linearization fit with a calculated LOD ± uncertainty of 80 ± 18 pg mL^{-1}. The dashed vertical line with gray shading indicates the limit of detection and its associated uncertainty.

Downloaded from pubs.acs.org/aecic7/article-pdf/doi/10.1021/acselectrochem.6c00175/6909763/ec-2026-00175f.pdf by guest on 06 November 2026

https://doi.org/10.1021/acselectrochem.6c00175
ACS Electrochem. XXXX, XXX, XXX−XXX

via drop-casting and a plate-based cTnI immunoassay where the TMB^+ product solution was subsequently transferred to the electrode. These formats were conducted under comparable experimental conditions to the chemisorption dataset, with the key difference being the degree of spatial control over antibody orientation and thus TMB^+ localization relative to the electrode surface.

To first assess baseline signal behaviour, total AUC was analysed independently of gradient cut-off thresholds (Figure 6). Absolute signal magnitude differed between formats (Figure 6A), with the plate-based configuration producing the largest responses and chemisorption the smallest. However, this did not translate directly to analytical performance.

Reproducibility analysis (Figure 6B) showed that the plate-based assay exhibited the lowest variability, reflecting consistent bulk TMB^+ generation, while physisorption showed high variability (mean ~25%, up to ~30%), consistent with heterogeneous antibody orientation. Chemisorption displayed moderate variability, indicating improved surface uniformity. Plotting RSD against total AUC (Figure 6D) highlights a clear trade-off between signal magnitude and precision.

Figure 6C depicts the normalized calibration curves, showing that physisorption had the largest signal response and an LOD of 81 pg mL^{-1}. Chemisorption normalized AUC signal was moderate, with low variability across all concentrations (LOD: 117.6 pg mL^{-1}). The plate-based dataset once normalized had a low signal response, and the LOD calculated was 1229 pg mL^{-1}. They exhibited greater normalized responses and lower background limits. Chemisorption normalized AUC signal was moderate, with low variability across all concentrations.

While the total AUC analysis produced reasonable calibration curves, it is expected that the most enriched area of the current time response will be within the temporal region, and clear differences may be seen between different immobilization strategies. Thus, gradient heatmap analyses were performed for the physisorption and plate-based datasets to define optimal cut-off ranges, with full heatmaps and corresponding dose−response curves provided in the Supporting Information (Figures S7−S14).

Clear immobilization-dependent differences were observed (Table 3). Physisorption produced the lowest LODs but also the highest variability (15.7 ± 7 pg mL^{-1} for the linear fit), consistent with enhanced sensitivity at the expense of increased scatter due to non-uniform antibody immobilization. As shown in Figure S11, the change in response between low and high concentrations contributes to the uncertainty in the calculated LOD. The 4PL model provided a more representative fit for this dataset, and the reported LODs have been updated

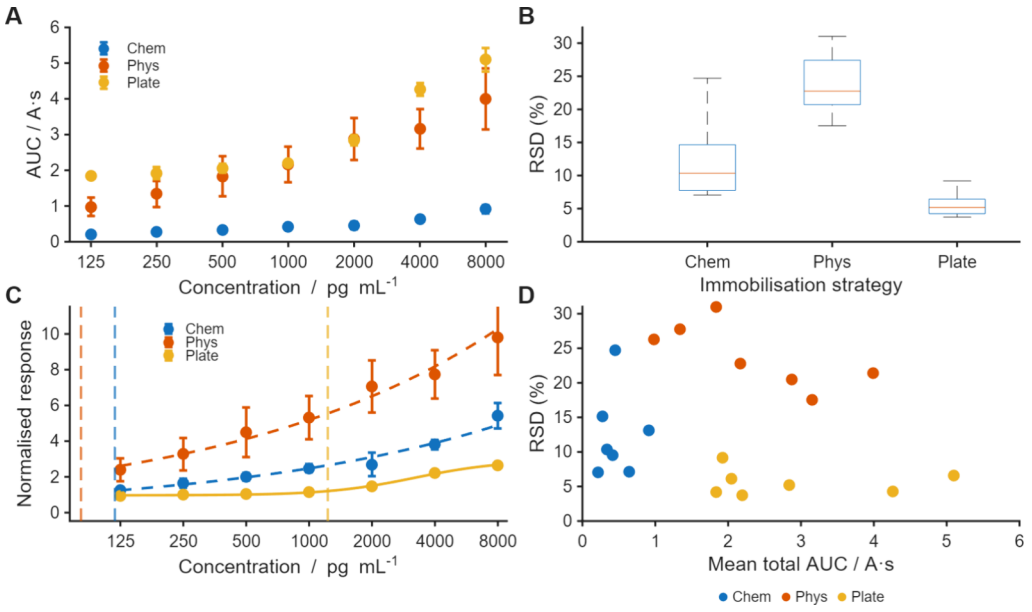

Figure 6. Comparison of signal magnitude, variability, and analytical performance across antibody immobilization strategies (chemisorption, physisorption, and plate-based electrochemical immunoassay) using total AUC analysis. (A) Mean total AUC versus cTnI concentration (±1 SD). (B) Relative standard deviation (RSD) across concentrations, showing reproducibility independent of signal magnitude. (C) Normalized AUC calibration curves with 4PL (solid line) or log−log linear fits (dashed lines); vertical dashed lines indicate LOD (±1 SD). (D) Relationship between signal magnitude and reproducibility (mean RSD vs mean AUC), highlighting trade-offs between sensitivity and precision.

Table 3. Comparison of Output of Gradient-Based AUC Integration across Immobilization Strategies: Physisorption, Chemisorption, and Bulk Solution[a]

immobilization	lower cutoff (nA s^{-1})	upper cutoff (nA s^{-1})	4PL fit LOD (pg mL^{-1})	linear fit LOD (pg mL^{-1})
chemisorption	20	75	46.0 ± 10	80.0 ± 18
physisorption	5	150	40.4 ± 3	15.7 ± 7
plate	50	150	1018 ±139	485.6 ±141

[a]Gradient cut-off screening heatmaps and the 4PL and linear fit comparison dose−response curves are available in the Supplemental Information.

https://doi.org/10.1021/acselectrochem.6c00175
ACS Electrochem. XXXX, XXX, XXX−XXX

Downloaded from pubs.acs.org/aecic7/article-pdf/doi/10.1021/acselectrochem.6c00175/6909763/ec-2026-00175f.pdf by guest on 06 November 2026

accordingly. Comparable variability was observed when the same experimental dataset was analysed using the steady-state approach,[11] indicating that the scatter is inherent to the physisorption system rather than introduced by the transient analysis method. Chemisorption operated over a broader gradient window (20−75 nA s^{-1}) and yielded more consistent LODs (80.0 ± 18 pg mL^{-1}). In contrast, the plate-based configuration required higher gradient thresholds (50−150 nA s^{-1}) and exhibited elevated LODs (1018 ± 139 pg mL^{-1}). These findings are consistent with literature correlating controlled immobilization on electrodes with improved assay precision.[23−25]

These trends support the hypothesis that immobilization strategy governs the spatial distribution of TMB^+ and, consequently, the information available during early transient. Chemisorption promotes localized redox generation at the electrode interface, producing a sharper and more reproducible initial response. Physisorption introduces heterogeneity but enables less hindered electron transfer, increasing sensitivity. In contrast, the plate-based format generates redox species in the bulk solution, resulting in diffusion-limited transport and a delayed current response, reducing the effectiveness of early-time signal isolation.

Comparison with the Limiting Current Approach

Table 4 compares the LODs obtained using the gradient-threshold AUC approach with those derived from the mean limiting current approach.

For chemically immobilized sensors, AUC-based analysis reduced the LOD from 130 to 80 pg mL^{-1}, corresponding to a 38.5% improvement. Physically immobilized sensors exhibited a substantially greater enhancement, with the LOD decreasing from 233 to 40.4 pg mL^{-1} (constituting with 82.7% reduction), highlighting the strong benefit of early-time signal extraction in controlled surface systems. In contrast, the plate-based format showed no improvement, with the LOD slightly increasing from 1000 to 1018 pg mL^{-1} (+1.8%), indicating that AUC-based analysis does not provide an advantage in diffusion-limited configurations. This comparison demonstrates that the power of early phase data analysis is strongly dependent on immobilization strategy. The results reinforce the mechanistic link between antibody immobilization, TMB^+ localization, and the chronoamperometric response, with surface-confined systems benefiting most from transient-based analysis.

To summarize, this work shows that analysing the early transient stage of the current−time response can improve the LOD in amperometric immunoassays. Across systems with different antibody immobilization strategies, the distribution of immunocomplexes and localization of redox species determined which regions of the signal carried the most analytical value. By selectively isolating these regions, the proposed framework enhanced performance for systems that used electrode functionalization. The improvement was evident in physically immobilized systems, where signal instability and non-specific interactions typically limit sensitivity when using limiting current as the analyte-determining variable. These findings highlight that targeted analysis of the transient response is a powerful and broadly applicable strategy for improving assay performance without increasing experimental complexity.

These improvements originate from focusing on the reaction-controlled portion of the current−time trace, where the signal is driven by the local concentration of the electroactive species generated by the enzymatic label, which depends on both analyte level and is particularly useful when electrode functionalization ensures close proximity to the electrode surface.

Conventional approaches based on fixed time points or extended integration windows do not account for this transition and incorporate regions dominated by capacitive artefacts or diffusion-limited behaviour, thus reducing sensitivity.[8] In contrast, the use of a gradient-based criterion allows selective isolation of the transient region, where the signal is governed by faradic current and less so by non-faradaic currents and background drift.[17]

The analysis also informs the calibration data fitting strategy. While 4PL curve-fitting is widely used in immunoassays, it requires a full sigmoidal response to ensure adequate robustness, which was not consistently observed within clinically relevant concentration ranges. In contrast, log−log linearization provided a more stable description of the low-concentration regime, where diagnostically relevant information is concentrated. Comparable LODs obtained from both approaches indicate that improvements in sensitivity arise primarily from signal extraction rather than the fitting model.

More broadly, this framework can be systematically harnessed to enhance sensitivity and robustness in biosensing applications. Particularly for real-world systems operating in complex biological matrices, where noise and variability limit the performance of traditional approaches. By providing a straightforward framework, this method offers a practical route toward improved diagnostic performance without requiring modification to assay chemistry, electrode design, or instrumentation.

Despite these advantages, there are some limitations to consider. For instance, analysis was limited by the amperometric ELISA immunoassay dataset which did not show a full sigmoidal dose response. At present, the method improves sensitivity but does not provide direct kinetic information such as binding rates. In addition, variability between electrodes, enzyme activity, and immobilization efficiency can still affect the results and should be thoroughly examined in future work.

Future work should focus on validating this approach across additional biomarkers and electrochemical systems to establish its broader applicability. The screening process could be

Table 4. Comparison of LODs Obtained from a Steady-State Current Approach and AUC of the Initial Burst Phase for Various Datasets[a]

immobilization	steady state LOD (pg mL^{-1})	AUC based LOD (pg mL^{-1})	percentage change LOD
chemisorption	130	80*	−38.5
physisorption	233	40.4**	−82.7
plate	1000	1018**	+1.8

[a]Selected LOD is the one in which the AUC data was best represented. Full data for the AUC fit is presented in Table 3. * log−log linearization analysis, ** 4PL analysis.

https://doi.org/10.1021/acselectrochem.6c00175
ACS Electrochem. XXXX, XXX, XXX−XXX

Downloaded from pubs.acs.org/aecic7/article-pdf/doi/10.1021/acselectrochem.6c00175/6909763/ec-2026-00175f.pdf by guest on 06 November 2026

optimized to include uncertainties. Further investigation of the underlying electrochemical processes, including the relative contributions of double-layer charging, faradaic reactions, mass transport and electron-transfer kinetics across the transient, could provide greater mechanistic understanding of the gradient-defined regions identified here.

■ CONCLUSIONS

This work challenges conventional limiting current analysis by demonstrating that integration of early transient chronoamperometric signal enhances sensitivity. Early-phase AUC analysis improved LODs for both chemisorbed (by 38.5%) and physisorbed (by 82.6%). Minimal improvement was observed for the plate-based format, indicating that transient analysis is less effective when signal generation is dominated by diffusion from the bulk phase.

These findings demonstrate that immobilization chemistry governs not only signal magnitude and reproducibility but also the electrochemical regime from which analytical information is most effectively extracted. Localized redox activity near the electrode surface favours transient-based analysis, whereas diffuse signal generation is better captured under steady-state conditions.

Importantly, this work establishes transient AUC integration as a generalizable analytical framework for electrochemical biosensing, enabling improved sensitivity and reduced measurement times without modification to assay chemistry or hardware. This approach provides both mechanistic insight and a practical route to enhancing performance in translation-oriented biosensor systems.

■ ASSOCIATED CONTENT

Supporting Information

The Supporting Information is available free of charge at https://pubs.acs.org/doi/10.1021/acselectrochem.6c00175.

Additional heatmap analysis, calibration data, and original current time traces (DOCX)

■ AUTHOR INFORMATION

Corresponding Author

Damion K. Corrigan − *Centre for Advanced Measurement Science and Health Translation, Pure and Applied Chemistry, University of Strathclyde, Thomas Graham Building, 295 Cathedral St., Glasgow G1 1XL, U.K.;* orcid.org/0000-0002-4647-7483; Email: Damion.corrigan@strath.ac.uk

Authors

Niamh Docherty − *Centre for Advanced Measurement Science and Health Translation, Pure and Applied Chemistry, University of Strathclyde, Thomas Graham Building, 295 Cathedral St., Glasgow G1 1XL, U.K.;* orcid.org/0009-0003-3047-8478

Ashton Theakstone − *Centre for Advanced Measurement Science and Health Translation, Pure and Applied Chemistry, University of Strathclyde, Thomas Graham Building, 295 Cathedral St., Glasgow G1 1XL, U.K.;* orcid.org/0000-0001-8754-5094

Dominik Duleba − *School of Chemistry, University College Dublin, Science Centre, South Belfield, Dublin 4, Ireland;* orcid.org/0000-0002-0618-2162

Matthew J Baker − *Centre for Advanced Measurement Science and Health Translation, Pure and Applied Chemistry, University of Strathclyde, Thomas Graham Building, 295 Cathedral St., Glasgow G1 1XL, U.K.; DxCover Ltd., 5 Robroyston Oval, Nova Technology Park, Glasgow G33 1AP, U.K.; School of Medicine and Dentistry, Faculty of Clinical and Biomedical Sciences, University of Central Lancashire, Preston PR1 2HE, U.K.*; Present Address: Cancer Research UK Scotland Institute, Garscube Estate, Switchback Road, Bearsden Glasgow G61 1BD, U.K.; orcid.org/0000-0003-2362-8581

Robert P. Johnson − *School of Chemistry, University College Dublin, Science Centre, South Belfield, Dublin 4, Ireland;* orcid.org/0000-0002-8046-2138

Complete contact information is available at: https://pubs.acs.org/doi/10.1021/acselectrochem.6c00175

Author Contributions

The manuscript was written through contributions of all authors. All authors have given approval to the final version of the manuscript.

Notes

The authors declare no competing financial interest.

■ ACKNOWLEDGMENTS

D.C. and N.D. thank the British Heart Foundation (BHF) for funding through a Translation Award (TA/F/23/210048). N.D. thanks Lillian Collins for assistance with data collection. N.D. thanks the National Measurement Laboratory for PhD sponsorship and co-supervisors Dr Susan Pang (National Measurement Laboratory (UK)) and Dr Ying Fu (University of Strathclyde). D.C. and R.J. acknowledge the JPIAMR Origami Sense Consortium Project for funding of their collaboration.

■ REFERENCES

(1) Tong, L.; Wu, L.; Su, E.; Li, Y.; Gu, N. Recent Advances in the Application of Nanozymes in Amperometric Sensors: A Review. *Chemosensors* **2023**, *11*, 233.

(2) Baracu, A. M.; Gugoasa, L. A. D. Review—Recent Advances in Microfabrication, Design and Applications of Amperometric Sensors and Biosensors. *J. Electrochem. Soc.* **2021**, *168*, 037503.

(3) Lisi, F.; Peterson, J. R.; Gooding, J. J. The application of personal glucose meters as universal point-of-care diagnostic tools. *Biosens. Bioelectron.* **2020**, *148*, 111835.

(4) Bollella, P. Enzyme-based amperometric biosensors: 60 years later … Quo Vadis?. *Anal. Chim. Acta* **2022**, *1234*, 340517.

(5) Corrigan, D. K.; Barhoum, A.; Altintas, Z. *Fundamentals of Sensor Technology*; Barhoum, A.; Altintas, Z., Eds.; Woodhead Publishing, **2023**; pp 239−264.

(6) El Hamdouni, Y.; Labjar, N.; Laasri, S.; Dalimi, M.; Labjar, H.; El Hajjaji, S. *Advancements in Voltammetry for Biosensing Applications*; Manjunatha, J. G., Ed.;Springer Nature, Singapore, **2025**; pp 461−482.

(7) Antiochia, R. Electrochemical biosensors for SARS-CoV-2 detection: Voltametric or impedimetric transduction?. *Bioelectrochemistry* **2022**, *147*, 108190.

(8) Bard, A. J.; Faulkner, L. R.; White, H. S. *Electrochemical Methods: Fundamentals and Applications*; John Wiley & Sons, **2022**.

Downloaded from pubs.acs.org/aecic7/article-pdf/doi/10.1021/acselectrochem.6c00175/6909763/ec-2026-00175f.pdf by guest on 06 November 2026

(9) Yaman, D.; Mani, V.; Ferreira-Gonzalez, S.; Corrigan, D. Disposable and cost-effective printed circuit board based sensing technology for rapid detection of alkaline phosphatase. *Microchem. J.* **2026**, *220*, 116656.
(10) Dobrea, A.; Blake, R.; Macdonald, D.; McKenzie, C.; Altmann, Y.; Corrigan, D. K.; Jimenez, M. WAFFLE − an automated platform for enhancing the performance of electrochemical biosensors. *Lab Chip* **2026**, *26*, 2035−2046.
(11) Docherty, N.; Collins, L.; Pang, S.; Fu, Y.; Milne, S.; Corrigan, D. Cost-effective Amperometric Immunosensor for cardiac troponin I as a step towards affordable point-of-care diagnosis of acute myocardial infarction. *Sens. Bio-Sens. Res.* **2025**, *47*, 100725.
(12) Rinaldi, C.; Corrigan, D. K.; Dennany, L.; Jarrett, R. F.; Lake, A.; Baker, M. J. Development of an Electrochemical CCL17/TARC Biosensor toward Rapid Triage and Monitoring of Classic Hodgkin Lymphoma. *ACS Sens.* **2021**, *6*, 3262−3272.
(13) Amatore, C.; Savéant, J. M.; Tessier, D. Charge transfer at partially blocked surfaces: A model for the case of microscopic active and inactive sites. *J. Electroanal. Chem. Interfacial Electrochem.* **1983**, *147*, 39−51.
(14) Pedersen, T.; Gurevich, L.; Magnusson, N. E.; Pedersen, T.; Gurevich, L.; Magnusson, N. E. Aspects of Electrochemical Biosensors Using Affinity Assays. *Biosensors* **2025**, *15*(3), 166.
(15) Docherty, N.; Miller, C. L.; Dobrea, A.; Macdonald, D.; Gordon, A.; Pang, S.; Fu, Y.; Jimenez, M.; Corrigan, D. K.; Patel, B. A. Development of a High-Sensitivity Electrochemical Immunoassay Using a Fully 3D-Printed Electrocatalytic Microelectrode Probe Platform. *Anal. Chem.* **2026**, *98* (12), 9260−9272.
(16) Wang, J. *Analytical Electrochemistry*; John Wiley & Sons, **2004**.
(17) Conceição, V. S.; Saraiva, D. P. M.; Denuault, G.; Bertotti, M. Calibration-Free Analysis with Chronoamperometry at Microelectrodes. *Anal. Chem.* **2024**, *96*, 14766−14774.
(18) Chen, J.; Li, C.; Zhu, W.; Peng, J.; Deng, X. An AUC-based impedance sensing method for rapid assessment of antioxidant compounds with NIH-3T3 cells cultured in a 16-well E-plate with integrated microelectrode arrays. *Sens. Actuators, B* **2019**, *283*, 390−398.
(19) Anson, F. C.; Osteryoung, R. A. Chronocoulometry: A convenient, rapid and reliable technique for detection and determination of adsorbed reactants. *J. Chem. Educ.* **1983**, *60*, 293.
(20) Steel, A. B.; Herne, T. M.; Tarlov, M. J. Electrochemical Quantitation of DNA Immobilized on Gold. *Anal. Chem.* **1998**, *70*, 4670−4677.
(21) Akanda, M. R.; Choe, Y.-L.; Yang, H. Outer-Sphere to Inner-Sphere" Redox Cycling for Ultrasensitive Immunosensors. *Anal. Chem.* **2011**, *84*, 1049−1055.
(22) Hughes, J. H.; Upton, R. N.; Reuter, S. E.; Phelps, M. A.; Foster, D. J. R. Optimising time samples for determining area under the curve of pharmacokinetic data using non-compartmental analysis. *J. Pharm. Pharmacol.* **2019**, *71*, 1635−1644.
(23) Chen, L.-C.; Wang, E.; Tai, C.-S.; Chiu, Y.-C.; Li, C.-W.; Lin, Y.-R.; Lee, T.-H.; Huang, C.-W.; Chen, J.-C.; Chen, W. L. Improving the reproducibility, accuracy, and stability of an electrochemical biosensor platform for point-of-care use. *Biosens. Bioelectron.* **2020**, *155*, 112111.
(24) Beitello, E.; Osei, K.; Kobulnicky, T.; Breausche, F.; Friesen, J. A.; Driskell, J. D. Oriented Surface Immobilization of Antibodies Using Enzyme-Mediated Site-Specific Biotinylation for Enhanced Antigen-Binding Capacity. *Langmuir* **2025**, *41*, 10576−10585.
(25) Huang, J.; Xie, Z.; Xie, L.; Luo, S.; Zeng, T.; Zhang, Y.; Zhang, M.; Wang, S.; Li, M.; Wei, Y.; Fan, Q.; Xie, Z.; Deng, X.; Li, D. Explore how immobilization strategies affected immunosensor performance by comparing four methods for antibody immobilization on electrode surfaces. *Sci. Rep.* **2022**, *12*, 22444.

Downloaded from pubs.acs.org/aecic7/article-pdf/doi/10.1021/acselectrochem.6c00175/69097663/ec-2026-00175f.pdf by guest on 06 November 2026

https://doi.org/10.1021/acselectrochem.6c00175
ACS Electrochem. XXXX, XXX, XXX−XXX